Chen, Min; Sukhomlinov, Dmitry; Taskinen, Pekka; Tiljander, Mia; Lindberg, Daniel; Jokilaakso, Ari

Phase relations of the MgO–SiO_2–CrO_x system at 1600°C in air and reducing atmospheres

Published in:
Journal of the American Ceramic Society

DOI:
10.1111/jace.19207

Published: 01/10/2023

Document Version
Publisher's PDF, also known as Version of record

Please cite the original version:
Chen, M., Sukhomlinov, D., Taskinen, P., Tiljander, M., Lindberg, D., & Jokilaakso, A. (2023). Phase relations of the MgO–SiO_2–CrO_x system at 1600°C in air and reducing atmospheres. *Journal of the American Ceramic Society*, *106*(10), 6230-6243. https://doi.org/10.1111/jace.19207

Received: 3 January 2023 | Revised: 1 May 2023 | Accepted: 1 May 2023

DOI: 10.1111/jace.19207

Journal of the American Ceramic Society

RESEARCH ARTICLE

Phase relations of the $MgO–SiO_2–CrO_x$ system at 1600°C in air and reducing atmospheres

Min Chen[1] | **Dmitry Sukhomlinov**[1] | **Pekka Taskinen**[1] | **Mia Tiljander**[2] | **Daniel Lindberg**[1] | **Ari Jokilaakso**[1]

[1]Department of Chemical and Metallurgical Engineering, School of Chemical Engineering, Aalto University, Espoo, Finland

[2]Geological Survey of Finland, Espoo, Finland

Correspondence
Ari Jokilaakso, Department of Chemical and Metallurgical Engineering, School of Chemical Engineering, Aalto University, Kemistintie 1F, P.O. Box 16100, FI-00076 Espoo, Finland.
Email: ari.jokilaakso@aalto.fi

Funding information
Aalto University, School of Chemical Engineering; Business Finland, Grant/Award Number: 2118452

Abstract

The equilibrium phase relations of the $MgO–SiO_2–CrO_x$ system were investigated at 1600°C in air and at pO_2 of 10^{-10} to 10^{-11} atm using a high-temperature isothermal equilibration technique followed by rapid quenching and direct phase composition analyses with electron probe X-ray microanalysis. Two-phase equilibria (liquid–cristobalite, liquid–spinel, liquid–corundum, and liquid–olivine) and three-phase equilibria (liquid–cristobalite–spinel, liquid–olivine–spinel, liquid–spinel–corundum, and cristobalite–spinel–corundum) were observed. The 1600°C isothermal sections at various oxygen partial pressures were constructed for the $MgO–SiO_2–CrO_x$ system based on the experimentally determined liquid and solid compositions. Data from the literature and the predictions by FactSage and MTDATA software were compared with the present experimental results.

KEYWORDS

chromium oxide, electrolytic ferrochromium, phase diagram, thermodynamics, waste management

1 | INTRODUCTION

The $MgO–Cr_2O_3$-based ceramics are widely used as refractories in high-temperature smelting furnaces due to their high melting points and high thermal stability.[1–3] In the smelter, the slag/refractory interaction has a vital effect on the lifespan of the refractories.[4] The stability of refractories in high-temperature smelting conditions can be predicted based on the phase relations in the $MgO–SiO_2–Cr_2O_3$ system since SiO_2 is a major component in most metallurgical slags.[5] Investigation of the phase relations of the $MgO–Cr_2O_3$-based system at different temperatures and oxygen partial pressures provides useful information on the stability of refractories under different smelting conditions.[6,7]

The production of FeCr alloy from ferrochrome mineral ores by molten oxide electrolysis (MOE)[8,9] is attractive due to the regulations for the emissions of greenhouse gases. In the MOE process, the chromite ore dissolves in the electrolyte (i.e., a molten oxide) and simultaneously undergoes electrolytic decomposition to liquid FeCr alloy and oxygen gas. Knowledge of the slag properties is critical for controlling the process operation. For example, slag foaming is linked with the formation of solid phases such as olivine and spinel. Furthermore, the stability of MgO-based refractories and the solubility of chromium in potential electrolyte slags can be determined by the phase equilibria of the $MgO–CrO_x$-based slag systems. Therefore, in the production of FeCr alloy from ferrochrome

---

ores by the MOE method, it is essential to control the primary phase field of the feed mixture at the operation temperature and oxygen partial pressures.[10–16]

The industrial stainless steel and ferrochromium slags conform with the SiO_2–CaO–MgO–Al_2O_3–Cr_2O_3–FeO_x system.[17–21] Different from argon oxygen decarburization stainless steel slags,[22–24] the slags from ferrochrome smelting are rather acidic, containing MgO and Al_2O_3 along with SiO_2 but without CaO.[25]

Various studies have been carried out on the phase equilibria of relevant subsystems including SiO_2–MgO,[26–30] SiO_2–Cr_2O_3,[31–34] and MgO–Cr_2O_3.[35,36] Regarding the MgO–SiO_2–Cr_2O_3 ternary system, Keith[37] determined the liquidus of the system at 1600°C–2100°C in air. Morita et al.[38–40] determined the primary phase field isotherms for the spinel in the MgO–SiO_2–CrO_x system at 1600°C in both air[38] and reducing atmosphere.[39,40] Their results obtained in air are in good agreement with the observations by Keith[37] and they[39,40] reported that the decrease of oxygen partial pressure led to an increase in the liquid domain. Li et al.[41] studied the subsolidus phase relations in the MgO–SiO_2–CrO_x system in equilibrium with metallic chromium at 1100°C–1500°C and 0–2.88 GPa. Arnout et al.[42] investigated the phase equilibria of the MgO–SiO_2–CrO_x system at 1600°C and pO_2 ranging from air to equilibrium with metallic chromium at a reducing atmosphere using a combined experimental and computational method. However, their experiments[42] were mainly conducted in the spinel primary phase field and only a limited effort was devoted to the cristobalite and forsterite (i.e., the olivine solid solution in this study) phase domains.

The aforementioned background indicates that the phase relations of the MgO–SiO_2–CrO_x system have not been investigated systematically, especially in reducing atmospheres. Therefore, the main purpose of this study is to determine the phase equilibria of the MgO–SiO_2–CrO_x system at 1600°C in air and at pO_2 of 10^{-10} to 10^{-11} atm using the well-established and accurate high-temperature equilibration/quenching method and phase composition analyses by electron probe X-ray microanalysis (EPMA). Investigation of the phase relations in the MgO–SiO_2–Cr_2O_3 subsystem provides insight into the dissolution of Cr_2O_3 from the stable chromite spinel[43,44] and simultaneously helps to operate the MOE process for controlling the feed mixture and the forming of freeze lining in the electrolyzer.

2 | EXPERIMENTAL

High-purity oxide powders of MgO (99.95 wt%), SiO_2 (99.995 wt%), and Cr_2O_3 (99.97 wt%), all from Alfa Aesar, were used to prepare the initial slag mixtures. Each oxide was weighed in an appropriate ratio, mixed in an agate

TABLE 1 The calculated gas flow rates at 1600°C for the various oxygen partial pressures.

Log_{10} [pO_2, atm]	CO (mL/min)	95% N_2–5% CO_2 (mL/min)	CO_2 (mL/min)
−10	488.5	–	11.5
−10	340.0	160.0	–
−11	440.0	60.0	–

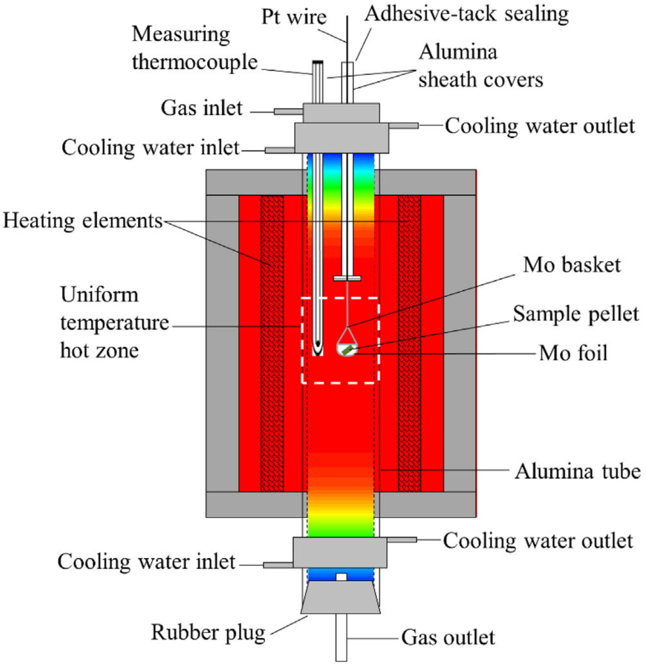

FIGURE 1 Schematic of the vertical equilibration tube furnace.

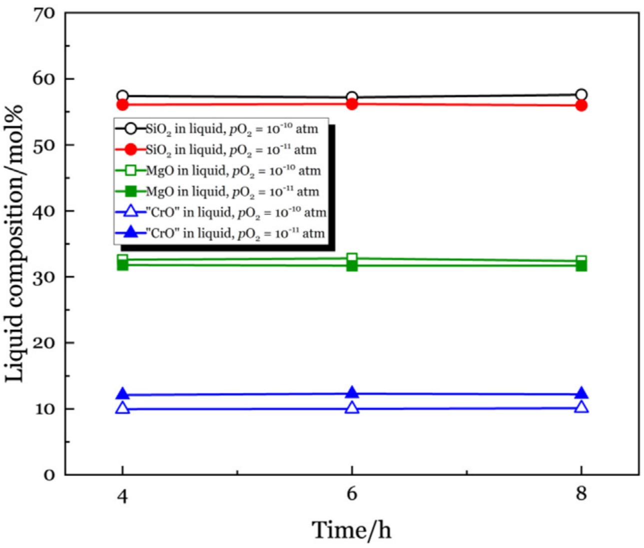

FIGURE 2 Concentrations of SiO_2, MgO, and "CrO" in liquid versus equilibration time.

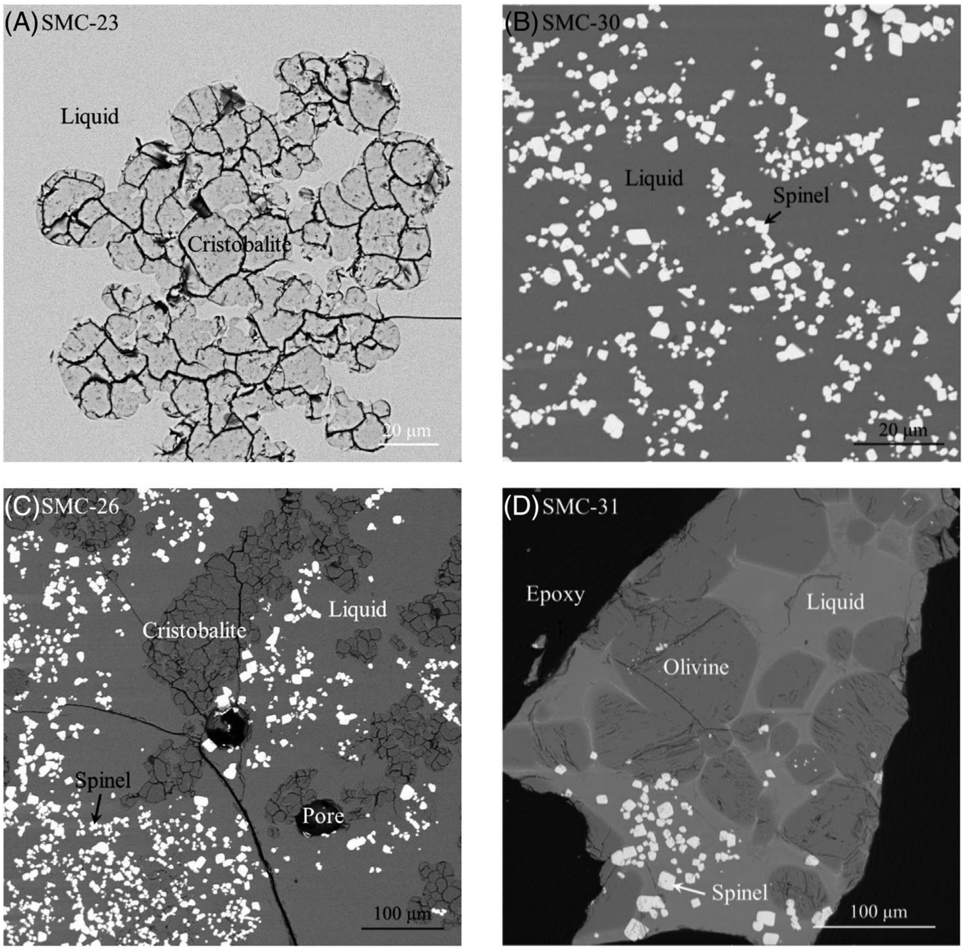

FIGURE 3 Typical microstructures of the $MgO-SiO_2-CrO_{1.5}$ system obtained at 1600°C in air: (A) liquid–cristobalite; (B) liquid–spinel; (C) liquid–spinel–cristobalite; (D) liquid–spinel–olivine phase fields.

mortar, and then pressed into a cylindrical pellet. The average weight of the sample was approximately 0.2 g. The gas atmosphere was controlled by adjusting the ratio of CO to CO_2 using the gas mixture of CO (99.97 vol%, AGA-Linde, Finland) and CO_2 (99.995 vol%, Woikoski Oy, Finland) or 95% N_2–5% CO_2 (Woikoski Oy). The target oxygen partial pressure and the gas flow rates were determined based on the following equations[45]:

$$2CO\,(g) + O_2\,(g) = 2CO_2\,(g) \tag{1}$$

$$\Delta G^{\theta}(\text{kJ/mol}) = -561.14 + 0.17T(\text{K}) \tag{2}$$

$$\lg\left(\frac{pO_2}{p^{\theta}}\right) = 2\lg\left(\frac{pCO_2}{pCO}\right) + \frac{0.434\Delta G^{\theta}}{RT} \tag{3}$$

where ΔG^{θ} refers to the standard Gibbs energy of reaction (1), T is the temperature (K), p^{θ} represents the standard atmospheric pressure of 1 bar. R is the gas constant of 8.314 J/(K mol). pO_2, pCO, and pCO_2 represent partial pressures of O_2, CO, and CO_2, respectively. Table 1 shows the calculated gas flow rates for the various oxygen partial pressures at 1600°C.

The experiments followed the procedure described in our previous studies.[46–48] The high-temperature isothermal equilibration experiments were conducted in a vertical Nabertherm furnace (Lilienthal, Germany, RHTV 120-150/1) equipped with $MoSi_2$ heating elements and a recrystallized alumina work tube. The sample temperature was measured using a calibrated S-type thermocouple (Johnson–Matthey Noble Metals, UK) placed next to the sample. DFC26 digital mass flow controllers (Aalborg, USA) were used to regulate the gas flow rates (see Table 1). Figure 1 shows the schematic diagram of the equilibration furnace. For the experiments in air, the sample pellets placed in the platinum crucible were lifted up to the furnace hot zone, whose lower end was open to ambient air. The experiments in reducing atmospheres were conducted in an envelope made of molybdenum foil. The sample pellets placed in a long molybdenum basket were lifted to the cold zone of the reaction tube using a platinum wire. Before equilibration, the lower end of the

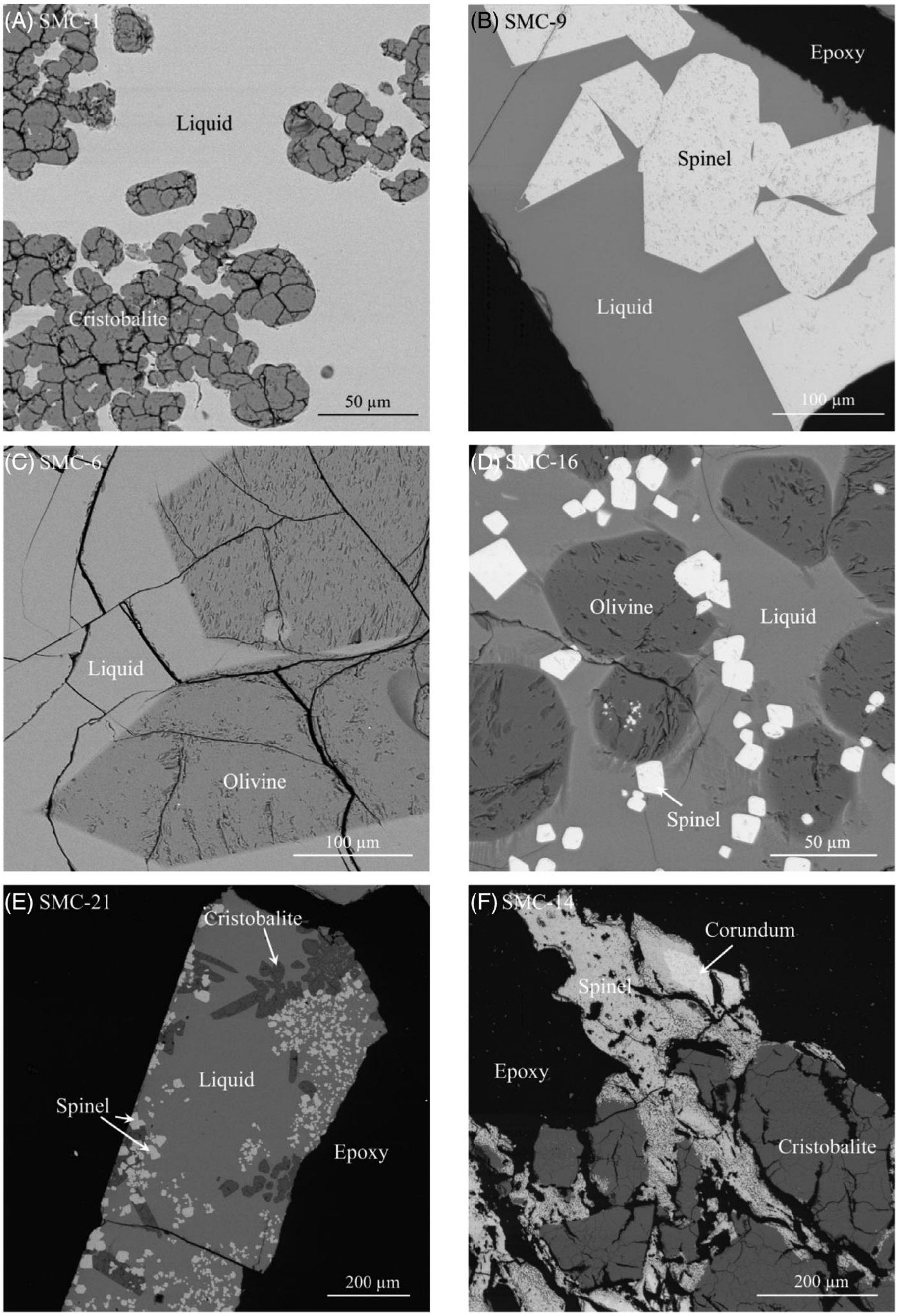

FIGURE 4 Back-scattered electron images of typical microstructures obtained at 1600°C and pO_2 of 10^{-10} atm: (A) liquid–cristobalite; (B) liquid–spinel; (C) liquid–olivine; (D) liquid–spinel–olivine; (E) liquid–spinel–cristobalite; (F) spinel–cristobalite–corundum.

reaction alumina work tube was sealed by a rubber plug, and a gas mixture for getting the target pO_2 at 1600°C was introduced into the furnace for approximately 30 min to stabilize the gas atmosphere. Subsequently, the sample was raised to the hot zone of the furnace for equilibration.

To determine the required time for reaching equilibrium liquid and solid compositions, time series experiments were conducted by annealing the samples with an initial high SiO_2 concentration (12.8 wt% Cr_2O_3–64.6 wt% SiO_2–22.6 wt% MgO) at 1600°C and pO_2 of 10^{-10} to 10^{-11} atm for 4, 6, and 8 h. The equilibration time was determined based on the stabilization of the concentrations of SiO_2, MgO, and "CrO" in liquid measured by energy-dispersive X-ray spectroscopy, as shown in Figure 2. Preliminary time-series experiments indicated that the system reaches equilibrium within 4 h at the experimental temperature. However, to ensure the equilibrium crystallization of solid phases, all samples were annealed at 1600°C in a controlled gas atmosphere for at least 8 h. After annealing, the sample was quenched into an ice–water mixture.

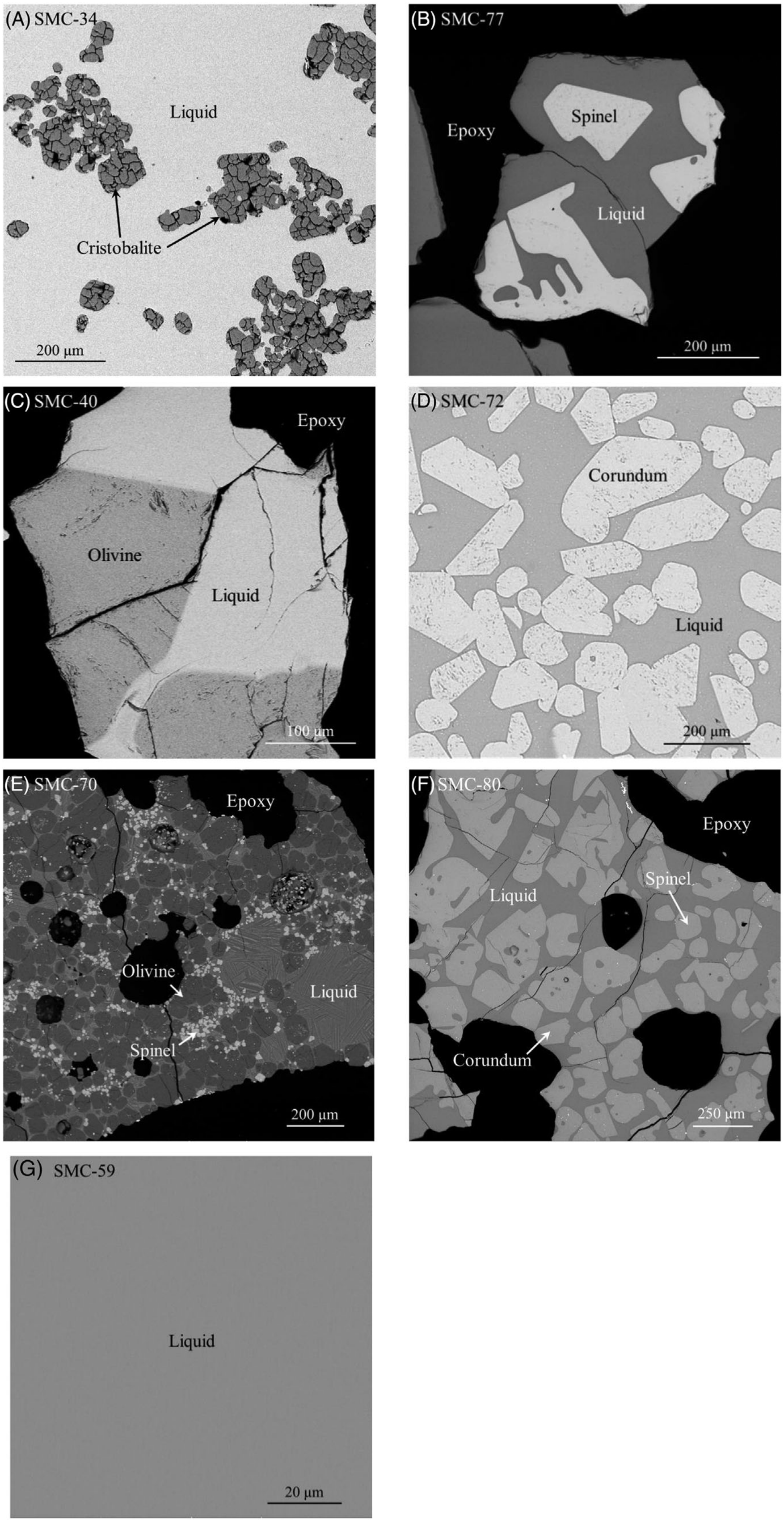

FIGURE 5 Back-scattered electron images of typical microstructures obtained at 1600°C and pO_2 of 10^{-11} atm: (A) liquid–cristobalite; (B) liquid–spinel; (C) liquid–olivine; (D) liquid–corundum; (E) liquid–spinel–olivine; (F) liquid–spinel–corundum; (G) single liquid equilibria.

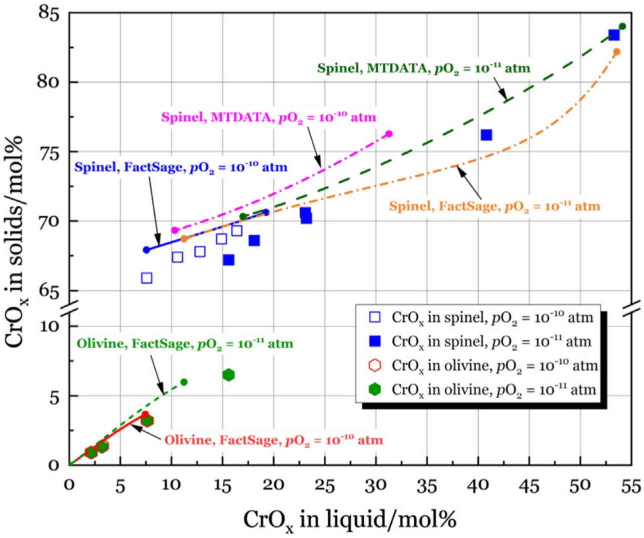

FIGURE 6 Solubility of CrO_x in olivine and spinel as a function of CrO_x concentration in the liquid.

The quenched samples were dried, mounted in epoxy, polished by wet metallographic methods, and carbon-coated using a carbon vacuum evaporator (JEOL IB-29510VET). The microstructures were determined using a Tescan Mira 3 scanning electron microscope (Tescan, Brno, Czech Republic) equipped with UltraDry silicon drift energy dispersive X-ray spectrometer (Thermo Fisher Scientific, Waltham, MA, USA). The direct measurement of phase compositions was conducted using a CAMECA (SX100) electron microprobe analyzer coupled with five wavelength-dispersive spectrometers with the following settings: accelerating voltage of 20 kV and beam current of 40 nA. A focused and a defocused beam diameter set to 5–20 μm were used. The external standards used in the EPMA analyses were diopside (Mg Kα), obsidian (O Kα), chromite (Cr Kα), and quartz (Si Kα). The PAP-ZAF program[49] was used for correcting the raw EPMA data. At least six analysis points were randomly selected from the well-quenched areas of each phase.

3 | RESULTS

The typical microstructures and the equilibrium phase compositions obtained at 1600°C in air and at pO_2 of 10^{-10} to 10^{-11} atm are shown in Figures 3–5 and Tables 2–4, respectively. The liquid–solid two-phase equilibria, including liquid–cristobalite, liquid–spinel, liquid–olivine, and liquid–corundum, and three-phase equilibria, including liquid–cristobalite–spinel, liquid–olivine–spinel, liquid–corundum–spinel, and cristobalite–spinel–corundum, were observed at 1600°C. The solid phases of olivine and spinel represent the solid solutions of $(Mg,Cr)_2SiO_4$ and $(Mg,Cr)Cr_2O_4$, respectively. While the solid phases of cristobalite and corundum represent the stochiometric phases of SiO_2 and Cr_2O_3, respectively. The analyzed concentrations of chromium obtained in air and reducing atmospheres were recalculated as "$CrO_{1.5}$" and "CrO", respectively.

As can be seen in Tables 3 and 4, the concentrations of CrO_x in olivine and spinel displayed a strong relationship with the liquid composition, as observed earlier in the literature.[44] Figure 6 shows the experimentally measured solubilities of CrO_x in the solid phases as a function of the CrO_x concentration in the liquid slag. The predictions by MTDATA and FactSage were also plotted onto the graph for comparison. It should be noted that both the experimental and the modeling points started and ended with three-phase equilibria except for the starting points for the olivine phase simulation results by FactSage. The experimentally determined solubilities of CrO_x in both spinel and olivine at pO_2 of 10^{-10} to 10^{-11} atm investigated in this study displayed an increasing trend with increasing CrO_x concentration in the liquid slag. The experimentally determined highest solubility of CrO_x in spinel increased from approximately 69–83 mol% with decreasing oxygen partial pressure from 10^{-10} to 10^{-11} atm. The decrease in oxygen partial pressure led to a decrease in CrO_x in spinel at a fixed CrO_x concentration in liquid, similar to the predictions by MTDATA. However, the present experimental results indicate that the increase in oxygen partial pressure from 10^{-11} to 10^{-10} atm had no significant effect on the dissolution of CrO_x in olivine, although the liquid phase equilibrated with olivine and spinel at pO_2 of 10^{-11} atm had higher CrO_x concentration than that determined at pO_2 of 10^{-10} atm.

The dissolution of CrO_x in olivine predicted by FactSage was close to the present experimental results, although the concentration of CrO_x in liquid in equilibrium with olivine and spinel at pO_2 of 10^{-11} atm by FactSage was approximately 4.5 mol% lower than the present results. The solubility data for CrO_x in olivine were not available in the MTDATA *Mtox* database (version 8.2). As for the spinel phase, the predicted maximum solubilities of CrO_x in spinel by MTDATA at pO_2 of 10^{-10} atm were around 76 mol%, which was higher than the present experimental results. At pO_2 of 10^{-11} atm, the experimentally determined maximum solubility of CrO_x in spinel was close to the calculations by MTDATA and FactSage. The dissolution of CrO_x in spinel predicted by FactSage at 1600°C and pO_2 of 10^{-10} atm was close to the present results.

4 | DISCUSSION

The 1600°C isothermal sections of the MgO–SiO_2–CrO_x phase diagram in air and at pO_2 of 10^{-10} to 10^{-11} atm were

TABLE 2 Equilibrium phase compositions for the $MgO–SiO_2–CrO_{1.5}$ system at 1600°C in air determined by electron probe X-ray microanalysis (EPMA).

Sample	Equilibrium phases	Equilibrium composition (mol%)		
		$CrO_{1.5}$	SiO_2	MgO
Liquid + cristobalite				
SMC-23	Liquid	0.1 ± 0.0	55.1 ± 0.3	44.8 ± 0.3
	Cristobalite	0.0 ± 0.0	100.0 ± 0.0	0.0 ± 0.0
SMC-24	Liquid	0.1 ± 0.0	56.0 ± 0.1	43.9 ± 0.1
	Cristobalite	0.0 ± 0.0	100.0 ± 0.0	0.0 ± 0.0
Liquid + spinel				
SMC-28	Liquid	0.8 ± 0.1	53.9 ± 0.1	45.3 ± 0.1
	Spinel	65.8 ± 0.3	0.1 ± 0.0	34.1 ± 0.3
SMC-30	Liquid	0.8 ± 0.1	50.4 ± 0.1	48.8 ± 0.1
	Spinel	65.6 ± 0.2	0.1 ± 0.0	34.3 ± 0.2
Liquid + cristobalite + spinel				
SMC-26	Liquid	1.0 ± 0.0	55.6 ± 0.2	43.4 ± 0.2
	Cristobalite	0.0 ± 0.0	99.9 ± 0.0	0.0 ± 0.0
	Spinel	65.7 ± 0.3	0.1 ± 0.0	34.3 ± 0.3
Liquid + olivine + spinel				
SMC-31	Liquid	0.5 ± 0.0	49.2 ± 0.1	50.3 ± 0.1
	Olivine	0.2 ± 0.0	33.2 ± 0.1	66.6 ± 0.1
	Spinel	65.4 ± 0.0	0.2 ± 0.1	34.4 ± 0.1

constructed based on the present experimental results, as shown in Figures 7–9, respectively. The present experimental results were compared with the predictions by FactSage (version 8.2) using the *FactPS* and *FToxid* databases[50,51] and by MTDATA with the *Mtox* database,[52,53] respectively.

4.1 | Construction of the 1600°C isotherm in air

Figure 7A shows the 1600°C isothermal section of the $MgO–SiO_2–CrO_{1.5}$ phase diagram in air constructed based on the present experimental results. The liquid domain and the primary phase fields of cristobalite, spinel, and olivine were constructed. The area marked in light gray was not investigated due to the limited experimental points. A comparison of the present experimental results and the data from the literature,[37,39,42] as shown in Figure 7B, indicates that the present liquid domain shrank toward the $MgO–SiO_2$ binary system when compared with the data by Keith[37] and Morita et al.[39] The primary phase field of spinel determined by Arnout et al.[42] had a similar chromium oxide concentration as the present study. Whereas the liquid composition point for the liquid–olivine–spinel coexisting equilibria determined by Arnout et al.[42] exhibited higher SiO_2 concentrations than the present results.

Figures 7C,D shows comparisons of the present observations and the simulations by FactSage and MTDATA, respectively. It can be seen in Figure 7C that the liquid domain determined in this study is narrower than the predictions by FactSage, shifting toward the area with a lower chromium oxide concentration. Figure 7D shows that the present liquid domain is close to the simulation by MTDATA, although the primary phase domain of spinel determined in this study displayed slightly lower chromium oxide concentrations than the predictions by MTDATA. The experimentally determined compositions of olivine and spinel in this study were close to the predictions by MTDATA and FactSage.

4.2 | Construction of the 1600°C isotherm at pO_2 of 10^{-10} atm

As shown in Figure 8A, the primary phase fields of cristobalite, spinel, and olivine were determined at 1600°C and pO_2 of 10^{-10}. The domains for liquid–cristobalite–spinel, liquid–olivine–spinel, and spinel–cristobalite–corundum three-phase coexisting equilibria were constructed based on the liquid and solid compositions. Based on the Gibbs phase rule, regions for olivine–spinel and cristobalite–spinel co-existing equilibrium can be constructed by connecting the solid composition points, although no

TABLE 3 Equilibrium phase compositions measured by electron probe X-ray microanalysis (EPMA) for the MgO–SiO_2–CrO_x system at 1600°C and pO_2 of 10^{-10} atm.

Sample	Equilibrium phases	Equilibrium composition (mol%)		
		"CrO"	SiO_2	MgO
Liquid + cristobalite				
SMC-1	Liquid	9.2 ± 0.1	56.2 ± 0.2	34.6 ± 0.1
	Cristobalite	0.1 ± 0.0	99.8 ± 0.1	0.1 ± 0.1
SMC-4	Liquid	5.3 ± 0.0	56.6 ± 0.2	38.2 ± 0.2
	Cristobalite	0.1 ± 0.0	99.9 ± 0.1	0.1 ± 0.1
SMC-5	Liquid	15.7 ± 0.0	55.3 ± 0.1	29.0 ± 0.1
	Cristobalite	0.2 ± 0.1	99.7 ± 0.1	0.1 ± 0.1
Liquid + spinel				
SMC-9	Liquid	14.9 ± 0.1	51.8 ± 0.4	33.3 ± 0.3
	Spinel	68.7 ± 0.2	0.0 ± 0.0	31.3 ± 0.2
SMC-10	Liquid	10.6 ± 0.1	48.3 ± 0.2	41.2 ± 0.2
	Spinel	67.4 ± 0.1	0.1 ± 0.0	32.5 ± 0.1
SMC-22	Liquid	12.8 ± 0.2	49.0 ± 0.3	38.3 ± 0.2
	Spinel	67.8 ± 0.4	0.1 ± 0.0	32.1 ± 0.4
Liquid + olivine				
SMC-6	Liquid	2.1 ± 0.0	47.3 ± 0.1	50.6 ± 0.1
	Olivine	0.9 ± 0.0	32.9 ± 0.1	66.2 ± 0.1
SMC-7	Liquid	3.3 ± 0.0	47.2 ± 0.2	49.5 ± 0.2
	Olivine	1.4 ± 0.0	32.8 ± 0.1	65.8 ± 0.1
SMC-8	Liquid	7.6 ± 0.0	45.7 ± 0.3	46.7 ± 0.2
	Olivine	3.2 ± 0.0	32.8 ± 0.1	64.0 ± 0.1
Liquid + olivine + spinel				
SMC-16	Liquid	7.6 ± 0.0	45.1 ± 0.1	47.3 ± 0.0
	Olivine	3.2 ± 0.1	32.9 ± 0.1	64.0 ± 0.1
	Spinel	65.9 ± 0.4	0.1 ± 0.0	34.0 ± 0.4
Liquid + cristobalite + spinel				
SMC-21	Liquid	16.4 ± 0.1	54.4 ± 0.2	29.2 ± 0.2
	Cristobalite	0.2 ± 0.0	99.7 ± 0.0	0.0 ± 0.0
	Spinel	69.3 ± 0.1	0.0 ± 0.0	30.7 ± 0.1
Cristobalite + corundum+ spinel				
SMC-14	Cristobalite	0.4 ± 0.1	99.5 ± 0.2	0.1 ± 0.1
	Spinel	71.6 ± 0.3	0.1 ± 0.2	28.3 ± 0.2
	Corundum	99.6 ± 0.2	0.4 ± 0.2	0.1 ± 0.0

experimental results were obtained in those areas in the present study.

The results for liquid–spinel and liquid–olivine–spinel equilibria determined by Arnout et al.[42] at 1600°C and pO_2 of $10^{-9.56}$ atm were close to the present results. However, the liquid point for liquid–spinel–cristobalite equilibrium by Arnout et al.[42] at 1600°C and pO_2 of $10^{-9.56}$ atm displayed relatively lower SiO_2 and "CrO" concentrations than the present study. Furthermore, the liquid composition for the liquid-cristobalite equilibrium by Arnout et al.[42] at 1600°C and pO_2 of $10^{-10.16}$ atm fitted well with the present observations. Their results for the spinel primary phase field shifted toward the area with higher "CrO" but lower SiO_2 concentrations when compared with the present experimental observations. The results for the liquid–spinel equilibrium determined by Morital et al.[39] at 1600°C and pO_2 of 2.73×10^{-10} atm displayed a similar trend to this study but they were shifted to a higher MgO concentration area.

TABLE 4 Equilibrium phase compositions obtained by electron probe X-ray microanalysis (EPMA) for the MgO–SiO_2–CrO_x system at 1600°C and pO_2 of 10^{-11} atm.

Sample	Equilibrium phases	Equilibrium composition (mol%)		
		"CrO"	SiO_2	MgO
Single liquid				
SMC-59	Liquid	26.2 ± 0.1	46.0 ± 0.2	27.8 ± 0.1
Liquid + cristobalite				
SMC-34	Liquid	4.8 ± 0.0	56.0 ± 0.0	39.2 ± 0.1
	Cristobalite	0.1 ± 0.0	99.9 ± 0.0	0.0 ± 0.0
SMC-35	Liquid	10.9 ± 0.0	54.8 ± 0.1	34.3 ± 0.1
	Cristobalite	0.2 ± 0.0	99.8 ± 0.0	0.0 ± 0.0
SMC-36	Liquid	16.6 ± 0.1	55.1 ± 0.1	28.2 ± 0.1
	Cristobalite	0.2 ± 0.1	99.8 ± 0.1	0.0 ± 0.0
SMC-73	Liquid	20.5 ± 0.1	54.2 ± 0.1	25.3 ± 0.1
	Cristobalite	0.3 ± 0.1	99.7 ± 0.1	0.0 ± 0.0
SMC-74	Liquid	37.3 ± 0.1	51.4 ± 0.1	11.3 ± 0.1
	Cristobalite	0.4 ± 0.0	99.6 ± 0.0	0.0 ± 0.0
SMC-75	Liquid	28.7 ± 0.2	52.9 ± 0.2	18.4 ± 0.2
	Cristobalite	0.4 ± 0.1	99.6 ± 0.1	0.0 ± 0.0
Liquid + spinel				
SMC-71	Liquid	18.1 ± 0.2	42.9 ± 0.1	39.0 ± 0.2
	Spinel	68.6 ± 0.3	0.0 ± 0.0	31.4 ± 0.3
SMC-76	Liquid	40.8 ± 0.2	41.9 ± 0.1	17.3 ± 0.1
	Spinel	76.2 ± 0.6	0.0 ± 0.0	23.8 ± 0.6
SMC-77	Liquid	23.2 ± 0.3	42.4 ± 0.1	34.3 ± 0.4
	Spinel	70.2 ± 0.5	0.0 ± 0.0	29.8 ± 0.5
SMC-79	Liquid	23.1 ± 0.4	42.7 ± 0.1	34.2 ± 0.5
	Spinel	70.6 ± 0.4	0.0 ± 0.0	29.4 ± 0.4
Liquid + olivine				
SMC-40	Liquid	2.2 ± 0.0	47.5 ± 0.0	50.3 ± 0.0
	Olivine	0.9 ± 0.0	32.9 ± 0.1	66.3 ± 0.1
SMC-41	Liquid	3.2 ± 0.0	47.8 ± 0.0	49.0 ± 0.0
	Olivine	1.3 ± 0.0	32.9 ± 0.1	65.7 ± 0.1
SMC-43	Liquid	7.7 ± 0.0	45.8 ± 0.1	46.4 ± 0.1
	Olivine	3.2 ± 0.0	32.9 ± 0.1	63.9 ± 0.1
Liquid + corundum				
SC-1	Liquid	57.7 ± 0.1	42.3 ± 0.1	0.0 ± 0.0
	Corundum	100.0 ± 0.0	0.0 ± 0.0	0.0 ± 0.0
SMC-72	Liquid	53.3 ± 0.5	42.2 ± 0.5	4.5 ± 0.2
	Corundum	99.9 ± 0.1	0.0 ± 0.0	0.0 ± 0.0
Liquid + corundum + spinel				
SMC-80	Liquid	53.3 ± 0.1	38.7 ± 0.1	8.0 ± 0.1
	Spinel	83.4 ± 0.1	0.0 ± 0.0	16.6 ± 0.1
	Corundum	100.0 ± 0.0	0.0 ± 0.0	0.0 ± 0.0
Liquid + olivine + spinel				
SMC-70	Liquid	15.6 ± 0.4	42.4 ± 0.2	42.0 ± 0.4
	Olivine	6.5 ± 0.1	33.0 ± 0.1	60.5 ± 0.1
	Spinel	67.2 ± 0.4	0.1 ± 0.0	32.6 ± 0.4

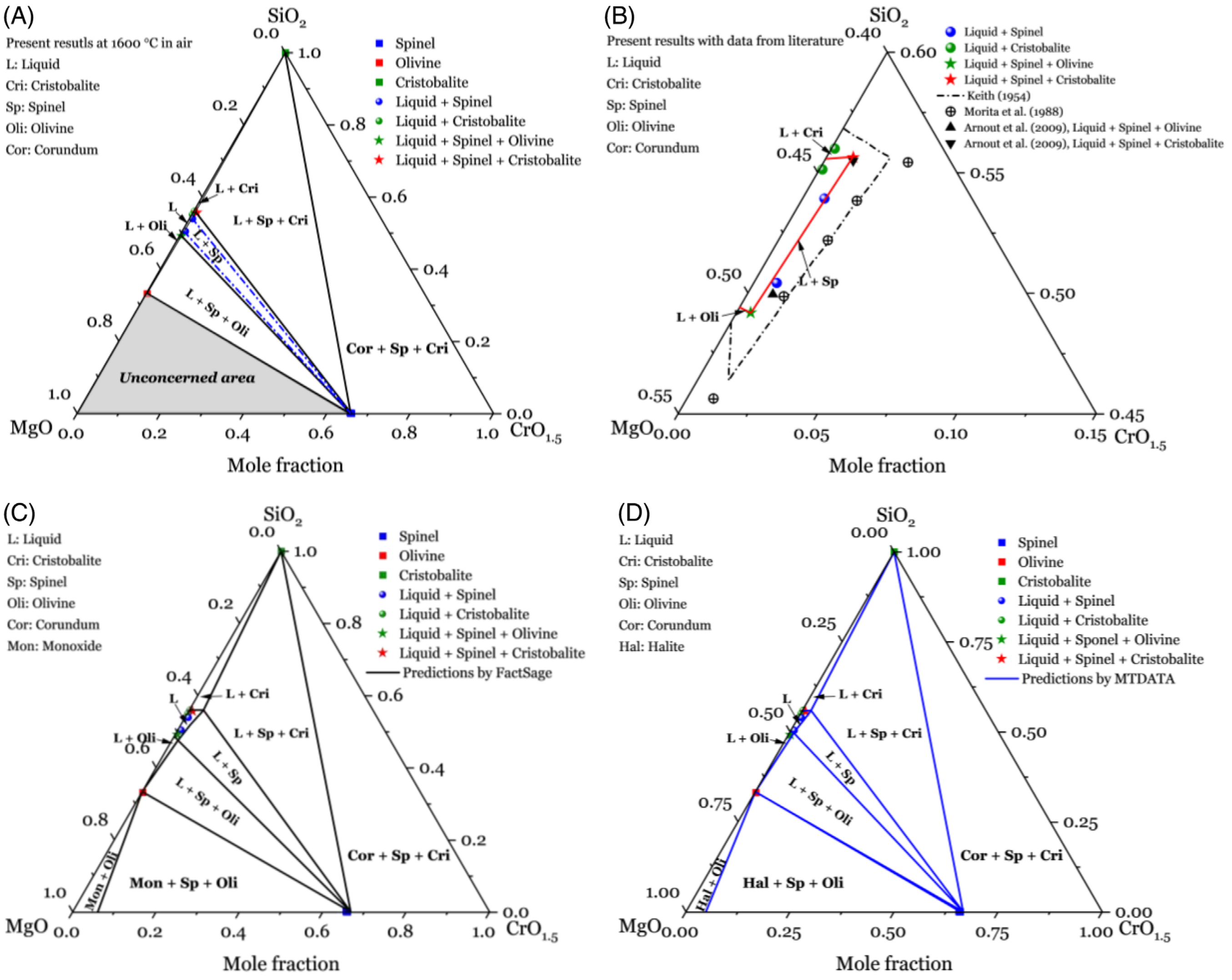

FIGURE 7 Isothermal section of the MgO–SiO$_2$–CrO$_{1.5}$ system at 1600°C in air: (A) the present results; (B) data from the literature[37,39,42]; (C) predictions by FactSage; (D) predictions by MTDATA. Halite of MTDATA is the same solid solution phase as monoxide in FactSage. The red line in Figure 4B represents the present experimental results.

Figure 8B shows that the liquid domain determined in the present study was close to the predictions by FactSage. The concentration of chromium oxide for the liquid point for the liquid–cristobalite–spinel three-phase coexisting equilibrium determined in this study was approximately 3 mol% lower than the calculation by FactSage. The domain for cristobalite–spinel equilibrium constructed in this study was narrower than the simulation by FactSage due to the lower experimentally determined dissolution of chromium oxide in spinel. Figure 8C shows that the liquid domain simulated by MTDATA deviated significantly from the present experimental results. The presence of the liquid–cristobalite–spinel three-phase equilibrium determined in this study contradicts the formation of the tie lines for liquid–corundum and the corresponding equilibria predicted by MTDATA and *Mtox* databases.

4.3 | Construction of the 1600°C isotherm at pO_2 of 10^{-11} atm

Figure 9A shows the present experimental results determined at pO_2 of 10^{-11} atm. Similar to the results at pO_2 of 10^{-10} atm, the primary phase fields of cristobalite, spinel, and olivine were constructed at 1600°C and pO_2 of 10^{-11} atm. However, the liquid–cristobalite–spinel and corundum–spinel–cristobalite three-phase equilibrium were not observed at pO_2 of 10^{-11} atm. Instead, the liquid–corundum and liquid–corundum–spinel phase domains were determined at pO_2 of 10^{-11} atm. The liquid domain enlarged significantly toward the area with a higher CrO_x concentration by decreasing oxygen partial pressure from 10^{-10} to 10^{-11} atm. The isotherm for the primary phase field of spinel determined at pO_2 of 10^{-11} atm exhibited

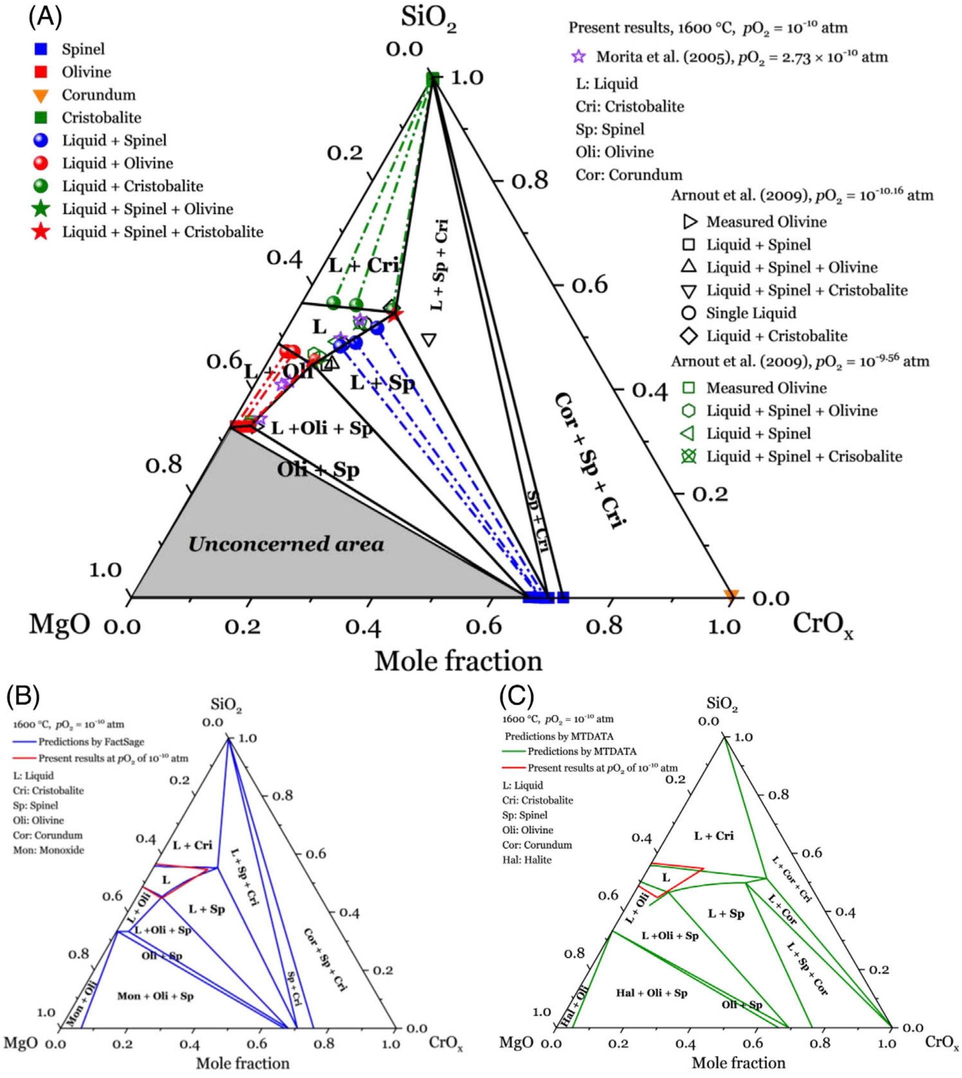

FIGURE 8 Isothermal section of the MgO–SiO$_2$–CrO$_x$ system at 1600°C and pO_2 of 10^{-10} atm: (A) the present results; (B) predictions by FactSage; (C) predictions by MTDATA. Halite of MTDATA represents the same solution phase as monoxide in FactSage.

a higher "CrO" concentration when compared with the present experimental results determined at pO_2 of 10^{-10} atm. The isotherm in the olivine primary phase field exhibited almost the same level of MgO concentration as the results at pO_2 of 10^{-11} atm, although the liquid phase in equilibrium with spinel and olivine at pO_2 of 10^{-11} atm displayed higher CrO$_x$ concentration than the results determined at pO_2 of 10^{-10} atm.

Figure 9B,C shows comparisons of the present experimental results and the calculated isothermal sections by FactSage and MTDATA, respectively. The liquid phase domain determined at 1600°C and pO_2 of 10^{-11} atm in this study was wider than the predictions by FactSage, as shown in Figure 9B. The isotherm for the olivine primary phase field calculated by FactSage fits well with the present experimental results, although the liquid point for the liquid–olivine–spinel three-phase equilibrium calculated by FactSage displayed a lower "CrO" concentration than the present observations. The isotherms in the spinel and corundum primary phase fields determined at 1600°C and pO_2 of 10^{-11} atm in this study displayed lower SiO$_2$ concentration than simulations by FactSage.

The primary field of olivine simulated by MTDATA expanded toward the area with higher SiO$_2$ concentrations than the present results and the computations by FactSage. The present isotherms in the cristobalite and spinel primary phase domains agreed well with simulations by MTDATA. The corundum primary phase domain determined in this study expanded toward the area with higher SiO$_2$ and MgO concentrations when compared with predictions by MTDATA.

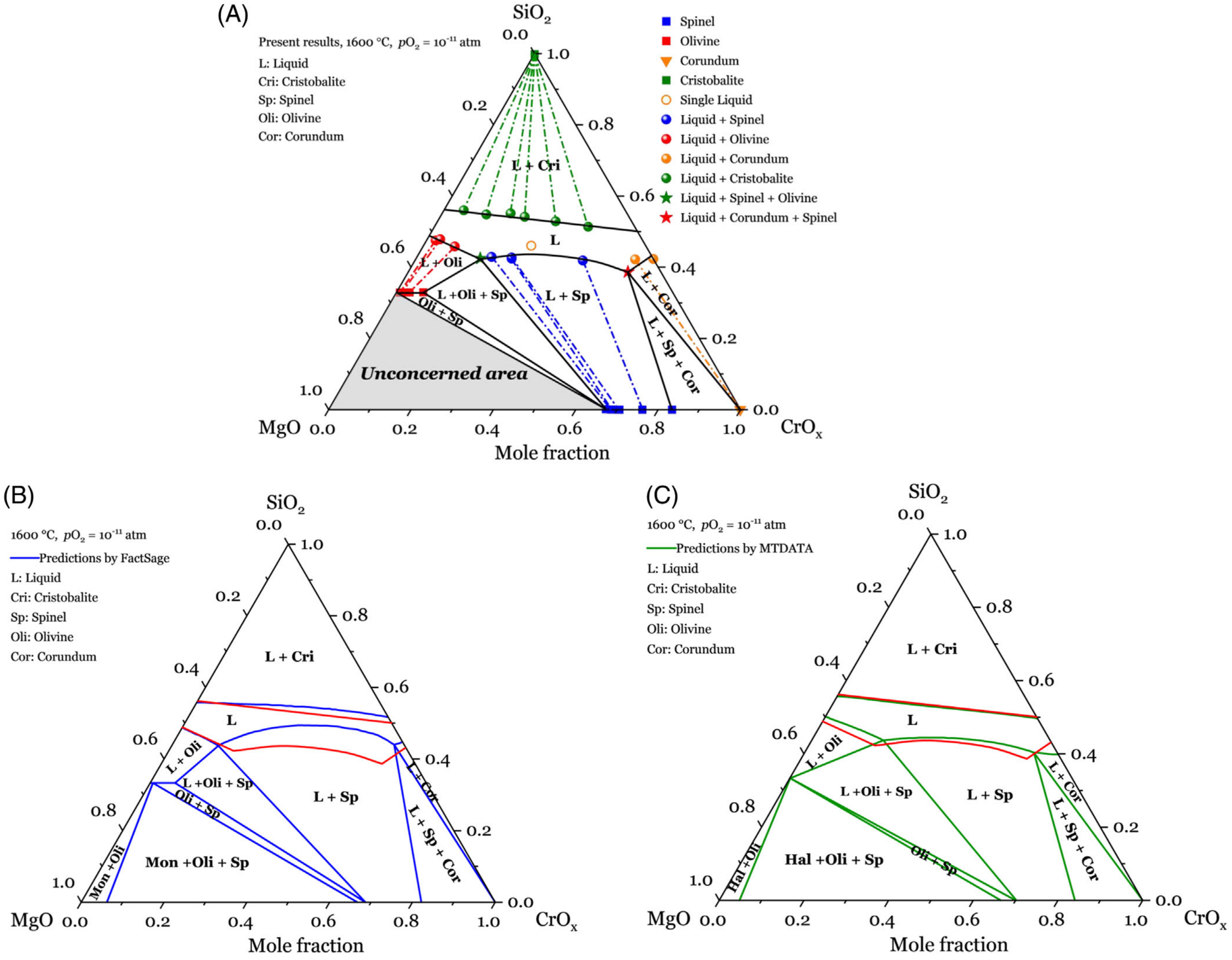

FIGURE 9 Isothermal section of the MgO–SiO_2–CrO_x system at 1600°C and pO_2 of 10^{-11} atm: (A) the present results; (B) predictions by FactSage; (C) predictions by MTDATA. Halite of MTDATA represents the same solution phase as monoxide in FactSage. The red lines in Figure 9B,C refer to the present experimental results.

5 | CONCLUSIONS

The equilibrium phase relations in the MgO–SiO_2–CrO_x system were investigated at 1600°C in air and reducing atmospheres of $pO_2 = 10^{-10}$ to 10^{-11} atm using the high-temperature isothermal equilibration/quenching/EPMA technique. Four two-phase primary phase fields (liquid–cristobalite, liquid–spinel, liquid–olivine, and liquid–corundum) and four three-phase regions (liquid–cristobalite–spinel, liquid–spinel–olivine, cristobalite–spinel–corundum, and liquid–corundum–spinel) were observed. The 1600°C isothermal sections of the MgO–SiO_2–CrO_x phase diagram in air and at pO_2 of 10^{-10} to 10^{-11} atm were constructed.

The present experimental results were compared with the data from literature and simulations by FactSage and MTDATA. The present experimental observations in air were close to the data reported in the literature and the computation by MTDATA. The present liquid domain obtained at pO_2 of 10^{-10} atm was closer to the calculations by FactSage than by MTDATA. The predicted liquidus domain in MTDATA extended to higher CrO_x and lower MgO compositions compared to the experimentally observed phase equilibria in this study. The present experimental results obtained at pO_2 of 10^{-11} atm were closer to the modeling by MTDATA than by FactSage. The difference between the simulations by MTDATA and FactSage was ascribed to the different databases and models used for the calculations. The present study indicates that the thermodynamic parameters in both databases should be re-assessed based on the present experimental data. The present results provide guidance for refractories corrosion, slag foaming, freeze-lining formation, and chromium extraction from ferrochrome ores and concentrates in the

MOE method by controlling the oxygen partial pressure and electrolyte slag composition.

ACKNOWLEDGMENTS

This work was partly financed by Aalto University, School of Chemical Engineering, and the TOCANEM project funded by Business Finland (grant number: 2118452). The utilization of the Academy of Finland's RawMatTERS Finland Infrastructure (RAMI) based at Aalto University, GTK Espoo, and VTT Espoo is acknowledged.

CONFLICT OF INTEREST STATEMENT

The authors declare no conflicts of interest.

ORCID

Min Chen https://orcid.org/0000-0003-0544-4359
Dmitry Sukhomlinov https://orcid.org/0000-0002-8752-4776
Pekka Taskinen https://orcid.org/0000-0002-4054-952X
Daniel Lindberg https://orcid.org/0000-0002-8442-1237
Ari Jokilaakso https://orcid.org/0000-0003-0582-7181

REFERENCES

1. Zargar HR, Oprea C, Oprea G, Troczynski T. The effect of nano-Cr_2O_3 on solid-solution assisted sintering of MgO refractories. Ceram Int. 2012;38(8):6235–41. https://doi.org/10.1016/j.ceramint.2012.04.077
2. Haldar MK, Tripathi HS, Das SK, Ghosh A. Effect of compositional variation on the synthesis of magnesite–chrome composite refractory. Ceram Int. 2004;30(6):911–5. https://doi.org/10.1016/j.ceramint.2003.10.012
3. Deng YY, Wang HZ, Zhao HZ. Influence of chrome-bearing sols vacuum impregnation on the properties of magnesia–chrome refractory. Ceram Int. 2008;34(3):573–80. https://doi.org/10.1016/j.ceramint.2006.12.002
4. Hon MH, Hsu CC, Wang MC. Reaction between magnesia-chrome brick/slag interface by electric furnace static slag corrosion test. Mater Trans. 2008;49(1):107–13. https://doi.org/10.2320/matertrans.MRA2007079
5. Yamaguchi A. Characteristics and problem of chrome-containing refractory. China's Refractories. 2007;16(3):3–7.
6. Muan A, Omiya S. Phase relations in the system iron oxide-Cr_2O_3 in air. J Am Ceram Soc. 1960;43(4):204–9. https://doi.org/10.1111/j.1151-2916.1960.tb12982.x
7. Ulmer GC, Smothers WJ. The system $MgO–Cr_2O_3–Fe_2O_3$ at 1300°C in air. J Am Ceram Soc. 1968;51(6):315–9. https://doi.org/10.1111/j.1151-2916.1968.tb15945.x
8. Zhou Z, Wang S, Jiao H, Jiao S. The feasibility of electrolytic preparation of Fe–Ni–Cr alloy in molten oxides system. J Electrochem Soc. 2017;164(14):D964. https://doi.org/10.1149/2.0711714jes
9. Sadoway DR. New opportunities for metals extraction and waste treatment by electrochemical processing in molten salts. J Mater Res. 1995;10(3):487–92. https://doi.org/10.1557/JMR.1995.0487
10. Gutiérrez-Paredes J, Romero-Serrano A, Plascencia-Barrera G, Vargas-Ramírez M, Zeifert B, Arredondo-Torres V. Chromium oxide reduction from slag by silicon and magnesium. Steel Res Int. 2005;76(11):764–8. https://doi.org/10.1002/srin.200506094
11. Velasco A, Ramírez M, Hernández S, Schmidt W, Revah S. Pilot scale treatment of chromite ore processing residue using sodium sulfide in single reduction and coupled reduction/stabilization processes. J Hazard Mater. 2012;207:97–102. https://doi.org/10.1016/j.jhazmat.2011.04.012
12. Zhao Q, Liu C, Cao L, Zheng X, Jiang M. Effect of lime on stability of chromium in stainless steel slag. Minerals. 2018;8(10):424. https://doi.org/10.3390/min8100424
13. Cao LH, Liu CJ, Zhao Q, Jiang MF. Effect of Al_2O_3 modification on enrichment and stabilization of chromium in stainless steel slag. J Iron Steel Res Int. 2017;24(3):258–65. https://doi.org/10.1016/S1006-706X(17)30038-9
14. Zeng Q, Li J, Mou Q, Zhu H, Xue Z. Effect of FeO on spinel crystallization and chromium stability in stainless steel-making slag. JOM. 2019;71(7):2331–7. https://doi.org/10.1007/s11837-019-03465-0
15. Song S, Tang D, Kumar D, Pistorius PC. Recycling of chromium-containing waste oxide as alloying addition in ladle metallurgy. Metall Mater Trans B. 2021;52(4):2612–8. https://doi.org/10.1007/s11663-021-02212-8
16. Wang D, Chen M, Jiang Y, Wang S, Zhao Z, Evans T, et al. Phase equilibria studies in the $CaO–SiO_2–Al_2O_3–MgO$ system with CaO/SiO_2 ratio of 0.9. J Am Ceram Soc. 2020;103(12):7299–309. https://doi.org/10.1111/jace.17421
17. Cao LH, Liu CJ, Zhao Q, Jiang MF. Analysis on the stability of chromium in mineral phases in stainless steel slag. Metall Res Technol. 2018;115(1):114. https://doi.org/10.1051/metal/2017071
18. Baciocchi R, Costa G, Di Bartolomeo E, Polettini A, Pomi R. Carbonation of stainless steel slag as a process for CO_2 storage and slag valorization. Waste Biomass Valoriz. 2010;1(4):467–77. https://doi.org/10.1007/s12649-010-9047-1
19. Fan WD, Yang QW, Guo B, Liu B, Zhang SG. Crystallization mechanism of glass–ceramics prepared from stainless steel slag. Rare Met. 2018;37(5):413–20. https://doi.org/10.1007/s12598-018-1030-1
20. Leuchtenmüller M, Antrekowitsch J, Steinlechner S. A kinetic study investigating the carbothermic recovery of chromium from a stainless-steel slag. Metall Mater Trans B. 2019;50(5):2221–8. https://doi.org/10.1007/s11663-019-01649-2
21. Fares AI, Sohel KMA, Al-Jabri K, Al-Mamun A. Characteristics of ferrochrome slag aggregate and its uses as a green material in concrete—a review. Constr Build Mater. 2021;294:123552. https://doi.org/10.1016/j.conbuildmat.2021.123552
22. Wang YJ, Zeng YN, Li JG, Zhang YZ, Zhang YJ, Zhao QZ. Carbonation of argon oxygen decarburization stainless steel slag and its effect on chromium leachability. J Cleaner Prod. 2020;256:120377. https://doi.org/10.1016/j.jclepro.2020.120377
23. Wang YJ, Zeng YN, Li JG, Zhang YZ, Wang W. Properties of ten-year-aged argon oxygen decarburization stainless steel slag. J Iron Steel Res Int. 2021;28(10):1233–42. https://doi.org/10.1007/s42243-021-00635-w
24. Baciocchi R, Costa G, Polettini A, Pomi R. Effects of thin-film accelerated carbonation on steel slag leaching. J Hazard Mater. 2015;286:369–78. https://doi.org/10.1016/j.jhazmat.2014.12.059

25. Niemelä P, Kauppi M. Production, characteristics and use of ferrochromium slags. In: INFACON XI. New Delhi, India: Indian Ferro Alloys Producers' Association; 2007. p. 171–9.
26. Bowen NL, Andersen O. The binary system $MgO–SiO_2$. Am J Sci. 1914;4(222):487–500. https://doi.org/10.2475/ajs.s4-37.222.487
27. Greig JW. Immiscibility in silicate melts: Part II. Am J Sci. 1927;13(74):133–54.
28. Schlaudt CM, Roy DM. Crystalline solution in the system $MgO–MgSiO_4–MgAl_2O_4$. J Am Ceram Soc. 1965;48(5):248–51. https://doi.org/10.1111/j.1151-2916.1965.tb14730.x
29. Hageman VB, Oonk HA. Liquid immiscibility in the SiO_2+MgO, SiO_2+SrO, $SiO_2+La_2O_3$, and $SiO_2+Y_2O_3$ systems. Phys Chem Glasses. 1986;27(5):194–8.
30. Abdeyazdan H, Shevchenko M, Hayes PC, Jak E. Integrated experimental and thermodynamic modeling investigation of phase equilibria in the $PbO–MgO–SiO_2$ system in air. Metall Mater Trans B. 2022;53(2):954–67. https://doi.org/10.1007/s11663-022-02440-6
31. Healy GW, Schottmiller JC. Chromium oxide–silica system at low oxygen pressures. Trans Metall Soc AIME. 1964;230(3):420–5.
32. Muan A. Equilibrium relations in systems containing chromium oxide, with a bearing on refractory corrosion in slagging coal gasifiers. High Temp High Pressures. 1982;14(6):653–60.
33. Degterov S, Pelton AD. Critical evaluation and optimization of the thermodynamic properties and phase diagrams of the $CrO–Cr_2O_3–SiO_2$ and $CrO–Cr_2O_3–SiO_2–Al_2O_3$ systems. J Phase Equilib. 1996;17(6):488–94. https://doi.org/10.1007/BF02665995
34. Shevchenko M, Shishin D, Jak E. Integrated phase equilibria experimental study and thermodynamic modeling of the Cr–Si–O, Fe–Cr–O and Fe–Cr–Si–O systems. Ceram Int. 2022;48(22):33418–39. https://doi.org/10.1016/j.ceramint.2022.07.286
35. Alper AM, McNally RN, Doman RC, Keihn FG. Phase equilibria in the system $MgO–MgCr_2O_4$. J Am Ceram Soc. 1964;47(1):30–3. https://doi.org/10.1111/j.1151-2916.1964.tb14636.x
36. Muller O, Roy R, White WB. Phase equilibria in the systems $NiO–Cr_2O_3–O_2$, $MgO–Cr_2O_3–O_2$, and $CdO–Cr_2O_3–O_2$ at high oxygen pressures. J Am Ceram Soc. 1968;51(12):693–9. https://doi.org/10.1111/j.1151-2916.1968.tb15930.x
37. Keith ML. Phase equilibria in the system $MgO–Cr_2O_3–SiO_2$. J Am Ceram Soc. 1954;37(10):490–6. https://doi.org/10.1111/j.1151-2916.1954.tb13981.x
38. Morita K, Shibuya T, Sano N. The solubility of the chromite in $MgO–Al_2O_3–SiO_2–CaO$ melts at 1600°C in air. Tetsu-to-Hagane. 1988;74(4):632–9. https://doi.org/10.2355/tetsutohagane1955.74.4_632
39. Morita K, Inoue A, Takayama N, Sano N. The solubility of $MgO–Cr_2O_3$ in $MgO–Al_2O_3–SiO_2–CaO$ slag at 1600°C under reducing conditions. Tetsu-to-Hagané. 1988;74(6):999–1005. https://doi.org/10.2355/tetsutohagane1955.74.6_999
40. Morita K, Tsukiashi K, Kimura M, Sano N. Activity of chromium oxide in $CaO–SiO_2$ based slags at 1873 K. Steel Res Int. 2005;76(4):279–83. https://doi.org/10.1002/srin.200506009
41. Li JP, Neill H, Seifert F. Subsolidus phase relations in the system $MgO–SiO_2$–Cr–O and thermodynamic properties of related Cr^{2+}-containing end-members. Acta Geol Sin. 1996;9(4):420–34. https://doi.org/10.1111/j.1755-6724.1996.mp9004008.x
42. Arnout S, Guo M, Jung IH, Blanpain B, Wollants P. Experimental determination of $CaO–CrO–Cr_2O_3–MgO–SiO_2$ and thermodynamic modeling of the $CrO–Cr_2O_3–MgO–SiO_2$ system. J Am Ceram Soc. 2009;92(8):1831–9. https://doi.org/10.1111/j.1551-2916.2009.03115.x
43. Albertsson G, Teng L, Björkman B, Seetharaman S, Engström F. Effect of low oxygen partial pressure on the chromium partition in $CaO–MgO–SiO_2–Cr_2O_3–Al_2O_3$ synthetic slag at elevated temperatures. Steel Res Int. 2013;84(7):670–9. https://doi.org/10.1002/srin.201200214
44. Li JL, Xu AJ, He DF, Yang QX, Tian NY. Effect of FeO on the formation of spinel phases and chromium distribution in the $CaO–SiO_2–MgO–Al_2O_3–Cr_2O_3$ system. Int J Miner Metall Mater. 2013;20(3):253–8. https://doi.org/10.1007/s12613-013-0720-9
45. Tian M, Wan X, Chen M, Taskinen P, Tiljander M, Jokilaakso A. Phase equilibria of $FeO_x–SiO_2–Al_2O_3$ slag system at 1200°C and pO_2 of $10^{-8.6}$ atm. Calphad. 2022;79:102502. https://doi.org/10.1016/j.calphad.2022.102502
46. Wan X, Shi J, Klemettinen L, Chen M, Taskinen P, Jokilaakso A. Equilibrium phase relations of $CaO–SiO_2–TiO_2$ system at 1400°C and oxygen partial pressure of 10^{-10} atm. J Alloys Compd. 2020;847:156472. https://doi.org/10.1016/j.jallcom.2020.156472
47. Chen M, Wan X, Shi J, Taskinen P, Jokilaakso A. Experimental study on the phase relations of the $SiO_2–MgO–TiO_2$ system in air at 1500°C. JOM. 2021;74(2):676–88. https://doi.org/10.1007/s11837-021-04870-0
48. Chen M, Wan X, Taskinen P, Sukhomlinov D, Shi J, Michallik R, et al. Phase equilibria in TiO_2-rich part of the $MgO–CaO–TiO_2$ system at 1500–1600°C. Ceram Int. 2022;48(14):20116–25. https://doi.org/10.1016/j.ceramint.2022.03.290
49. Pouchou JL, Pichoir F. Basic expression of "PAP" computation for quantitative EPMA. In: Brown JD, Packwood RH, editors. 11th International Congress on X-Ray Optics and Microanalysis (ICXOM). 1986. p. 249–53.
50. Bale CW, Bélisle E, Chartrand P, Decterov SA, Eriksson G, Hack K, et al. FactSage thermochemical software and databases-recent developments. Calphad. 2009;33(2):295–311. https://doi.org/10.1016/j.calphad.2008.09.009
51. Jung IH, Van Ende MA. Computational thermodynamic calculations: FactSage from CALPHAD thermodynamic database to virtual process simulation. Metall Mater Trans B. 2020;51(5):1851–74. https://doi.org/10.1007/s11663-020-01908-7
52. Davies RH, Dinsdale AT, Gisby JA, Robinson JAJ, Martin AM. MTDATA-thermodynamic and phase equilibrium software from the national physical laboratory. Calphad. 2002;26(2):229–71. https://doi.org/10.1016/S0364-5916(02)00036-6
53. Gisby J, Taskinen P, Pihlasalo J, Li Z, Tyrer M, Pearce J, et al. MTDATA and the prediction of phase equilibria in oxide systems: 30 years of industrial collaboration. Metall Mater Trans B. 2017;48(1):91–8. https://doi.org/10.1007/s11663-016-0811-x

How to cite this article: Chen M, Sukhomlinov D, Taskinen P, Tiljander M, Lindberg D, Jokilaakso A. Phase relations of the $MgO–SiO_2–CrO_x$ system at 1600°C in air and reducing atmospheres. J Am Ceram Soc. 2023;106:6230–6243. https://doi.org/10.1111/jace.19207